Tailoring Alphabetical Metamaterials in Optical Frequency: Plasmonic Coupling, Dispersion, and Sensing

Jun Zhang,[†] Cuong Cao,[†,#] Xinlong Xu,[‡] Chihao Liow,[§] Shuzhou Li,[§,*] PingHeng Tan,[∥,*] and Qihua Xiong[†,⊥,*]

[†]Division of Physics and Applied Physics, School of Physical and Mathematical Sciences, Nanyang Technological University, Singapore 637371, [‡]Nanobiophotonic Center, State Key Lab Incubation Base of Photoelectric Technology and Functional Materials, Institute of Photonics & Photon-Technology, Northwest University, Xi'an 710069, China, [§]Division of Materials Science, School of Materials Science and Engineering, Nanyang Technological University, Singapore 639798, [∥]State Key Laboratory of Superlattices and Microstructures, Institute of Semiconductors, Chinese Academy of Sciences, Beijing 100083, China, and [⊥]NOVITAS, Nanoelectronics Centre of Excellence, School of Electrical and Electronic Engineering, Nanyang Technological University, Singapore, 639798. [#]Present address: Institute for Global Food Security, School of Biological Sciences, Queen's University, Belfast BT9 5AG, UK.

ABSTRACT Tailoring optical properties of artificial metamaterials, whose optical properties go beyond the limitations of conventional and naturally occurring materials, is of importance in fundamental research and has led to many important applications such as security imaging, invisible cloak, negative refraction, ultrasensitive sensing, and transformable and switchable optics. Herein, by precisely controlling the size, symmetry, and topology of alphabetical metamaterials with U, S, Y, H, U-bar, and V shapes, we have obtained highly tunable optical response covering visible-to-infrared (vis-NIR) optical frequency. In addition, we show a detailed study on the physical origin of resonance modes, plasmonic coupling, the dispersion of resonance modes, and the possibility of negative refraction. We have found that all the electronic and magnetic modes follow the dispersion of surface plasmon polaritons; thus, essentially they are electronic- and magnetic-surface-plasmon-polaritons-like (ESPP-like and MSPP-like) modes resulted from diffraction coupling between localized surface plasmon and freely propagating light. On the basis of the fill factor and formula of magnetism permeability, we predict that the alphabetical metamaterials should show the negative refraction capability in visible optical frequency. Furthermore, we have demonstrated the specific ultrasensitive surface enhanced Raman spectroscopy (SERS) sensing of monolayer molecules and femtomolar food contaminants by tuning their resonance to match the laser wavelength, or by tuning the laser wavelength to match the plasmon resonance of metamaterials. Our tunable alphabetical metamaterials provide a generic platform to study the electromagnetic properties of metamaterials and explore the novel applications in optical frequency.

KEYWORDS: alphabetical metamaterials · optical frequency · tunable optical response · plasmonic coupling · surface plasmon polaritons · surface enhanced Raman spectroscopy (SERS)

Plasmonics has attracted considerable interest over the past decades due to its capabilities in manipulation and concentration of light into subwavelength volume based upon the surface plasmons (SPs).[1] SPs are collective charge oscillations on the surface of conductor in the presence of a two-dimensional (2D) boundary.[2] In the view of quantum mechanics, SPs are one type of quasi-particles or waves that propagate along the surface. When the phase velocity of SPs is comparable to the velocity of light, SPs resonantly couple with the free electromagnetic field and forms a new surface plasmon polaritons (SPPs).[2−4] Consequently, the SPPs bridge a gap between photons and collectively charge oscillations, since SPPs can convert light into intense and localized field distributions with SPs propagated over tens of micrometers, or convert back to the freely propagating light. Therefore, the SPPs can serve as a basis for constructing nanoscale photonic circuits that will be able to carry optical signals and electric currents.[3] Second, the use of SPPs and SPs can concentrate light in subwavelength structures stemming from the different (relative) permittivities of the metals and the surrounding nonconducting media.[3,5−8] Concentrating light in this way leads to an electric field enhancement that can be used to manipulate light−matter interactions or boost nonlinear phenomena, enabling superior applications in sensing.[3]

* Address correspondence to lisz@ntu.edu.sg, phtan@semi.ac.cn, Qihua@ntu.edu.sg.

Received for review January 26, 2014 and accepted March 26, 2014.

Published online March 26, 2014
10.1021/nn500527f

For instance, metallic structures that are much smaller than the wavelength of light can be used as substrates for surface-enhanced Raman spectroscopy (SERS), which can now detect a single molecule.[9−12]

The properties of SPs and SPPs strongly depend on the optical parameters and morphology of plasmonic structures. In the past 15 years, metamaterials have been gradually emerging as a material of choice for designing functional plasmonic structures because their optical properties can be tailored almost at will from microwave to optical frequency.[13−17] Metamaterials are artificial materials consisting of self-similar and periodically arranged metallic nanostructures which act as "artificial atoms" analogous to their natural counterparts in solid state physics. Therefore, optical properties of the metamaterials are strongly dependent on their size, periodicity, structural symmetry of the unit cells, and coupling between the metallic "atoms". Especially, the coupling effects play an important role in the understanding of the plasmonic modes from individual metallic elements to the bulk metamaterials.[18,19] It is similar to the molecule hybridization effects in solid state physics, in which the electronic states are evolved from individual electronic level in atoms to continuum band in bulk; the plasmonic coupling effect between the subwavelength metallic elements also dominates over the evolution of resonant modes in metamaterials.[20,21] Besides the electronic surface plasmons (ESPs) induced by charged oscillation, some metamaterials structures, such as "split ring resonator", also show a magnetic surface plasmons (MSPs), essentially analogous to a small *LC* circuit consisting of an inductance *L* and a capacitance *C*.[17,22] Near the resonance of MSPs, the current in the inductance produces a magnetic field opposing the external magnetic field of the light, hence enabling a negative magnetic permeability. Furthermore, the coupling between light and both of ESPs and MSPs will form two types of polaritons: electronic surface plasmon polaritons (ESPPs) and magnetic surface plasmon polaritons (MSPPs) that are analogue of the magnon-polaritons in antiferromagnetic materials.[23] By properly designing these parameters, one can tailor optical properties of metamaterials and exhibit unprecedented properties that the materials in nature cannot have, such as negative refraction, controllable optical illusions (*e.g.*, invisibility cloak), control of the polarization and spin of light, and enhanced nonlinear effect, as well as extreme light concentration for ultrasensitive sensing.[1,7,16,17,22,24−26]

Although much effort has been dedicated in this field over the past 15 years, a detailed study on the tunability and control of the SPs and SPPs in metamaterials is needed, especially on pushing the optical resonance into the visible-near-infrared (vis-NIR) wavelengths.[15,27,28] Herein, we use alphabetical metamaterials as a model to present a systematic study on the tailoring of optical response in vis-NIR frequency. First, we show the fabrication of alphabetical metamaterials, physical origin of resonance modes, and the plasmonic coupling effects induced by symmetry and size of resonators. Then, we discuss the dispersion relationship of resonance modes which follow the dispersion curves of 2D surface plasmon polaritons; thus, they have SPP-like properties. On the basis of the dispersion properties, we conclude that the SPP-like modes and SPs in our alphabetical metamaterials have low group velocity, which means that those metamaterials should have good capabilities in coupling the localized field (surface plasmon) and the propagation field (light), leading to strong field confinement and enhancement.[2,7] Finally, we use SERS techniques to demonstrate that those metamaterials have very good potential in the ultrasensitive bio/chemical sensing.

RESULTS AND DISCUSSION

Identification of Resonance Modes and Coupling Effect in Alphabetical Metamaterials. Figure 1 shows a series of alphabetical metamaterial structures (Figure 1a), their optical responses (Figure 1b), and mode identifications (Figure 1c). The fabrication details and structure parameters can be found in Methods and Supporting Information (Figure S1). In order to obtain the tunable optical response from visible to NIR range, we shrink the whole unit cell along with the dimension of resonators from 100% to 37.5%, which reduces the corresponding bar width (w) from w = 80 to 30 nm (Figure S1). Figure 1b shows the transmission spectra for various alphabetical metamaterials with different widths, w. The solid curves are spectra taken under P_x polarization configurations, while the dashed curves are obtained from P_y polarization configurations. Each valley in the transmission spectra represents one resonance mode of metamaterials. The induced electric dipoles due to the alternating field of light lead to two distinct resonance modes: one is electric mode arising from oscillation of the electric dipoles, while the other is the magnetic mode due to the circular currents induced by head-to-end electric dipoles configuration.[18,29] For all six shapes, the weak short-wavelength resonances around 550 nm exhibit independence on the width, which are actually attributed as the dipole excitation along the width of arms and their frequency depend on the ratio of arm length to arm width.[14,16,30] In our experiments, we change the size of metamaterials by shrinking the size of whole unit cell; thus, the ratio of arm length to arm width is constant. As a result, the modes around 550 nm exhibit no dependence on the apparent resonator arm. The other resonance modes exhibit a systematic blue shift as the width decreases, labeled with color lines as guide to eye. This can be explained as follows. For the electric modes, resonance frequency is proportional to the coupling strength of electric dipoles.[29,31] With a decrease in the

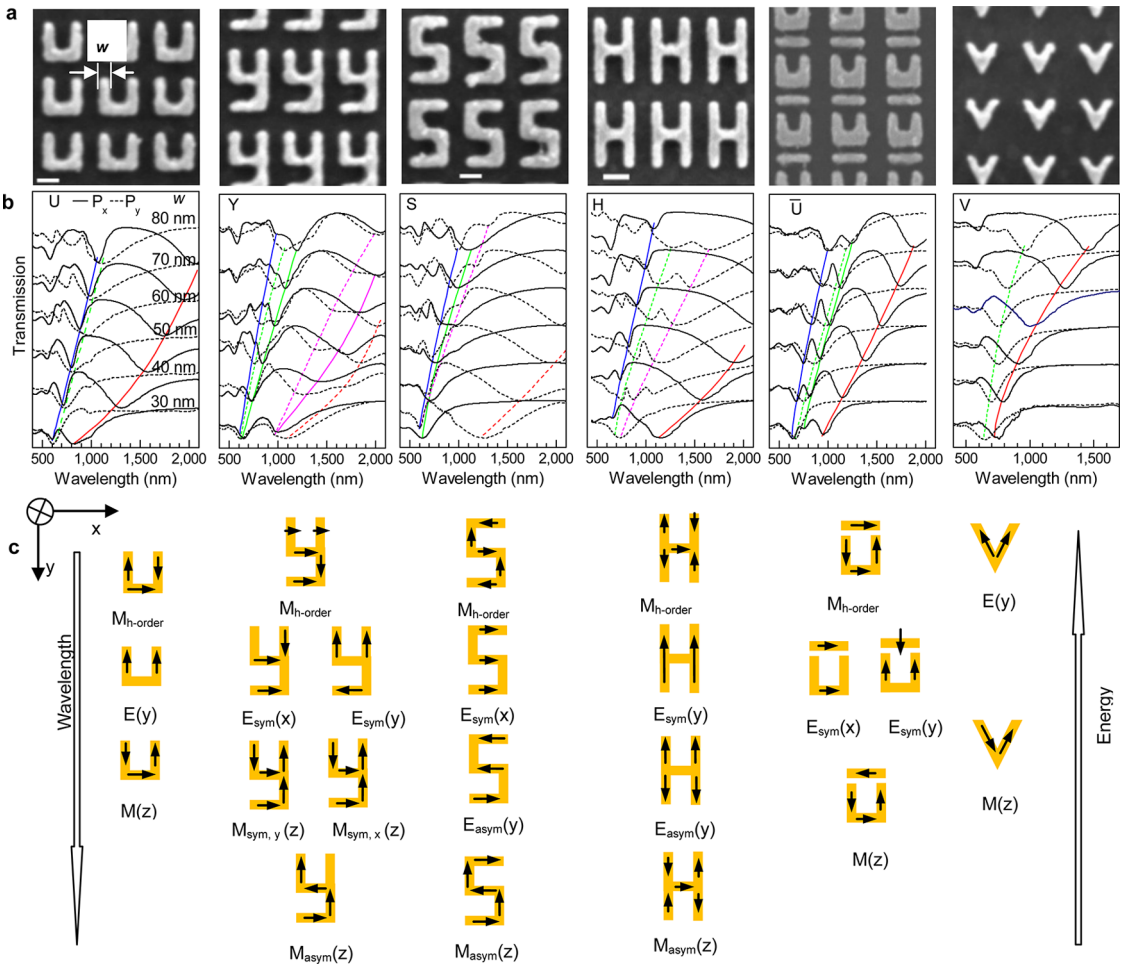

Figure 1. SEM images, transmission spectra and schematic diagrams of the plasmon hybridization. (a) A typical SEM images of U, Y, S, H, U-bar, and V shaped gold metamaterials with $w = 40$ nm fabricated on a flexible PEN or ITO/glass substrate. The scale bar is 100 nm in the figure. (b) Transmission spectra of SRRs with different widths of $w = 80-30$ nm for U, Y, S, H, U-ba,r and V shapes. The solid curves correspond to the P_x polarization, while the dashed curves correspond to the P_y polarization. The color lines highlight the trends of resonance depending on the size of unit. (c) Dipole current distribution of the plasmon hybridization modes for different shapes. For each shape, the modes are arranged by the order of wavelength (energy), with two degenerate cased for Y and U-bar shapes. The corresponding simulated results can be found in Figure S2. For electronic modes, the label in the brackets correspond the polarization direction of incident light; for magnetic modes, it is direction of magnetic moment.

metamolecule width, the coupling strength and, thus, the resonance frequency increases. The magnetic mode can be seen as the analogy of inductor–capacitor circuit (LC) resonance.[16] With the decrease of the metamolecule size and bar width, the capacitance C and inductance L decrease and the resonance frequency increases. Figure 1c shows the schematic diagram of the current distribution at the resonance wavelength based on the simulation of finite-difference-time-domain (FDTD) and dipole–dipole coupling theory.[18,29] The black arrows in Figure 1c indicate the dipole–current direction. The detailed FDTD simulation results of 30 nm width are shown in Figure S3. The simulated mode numbers, polarization, and relative energy are in good agreement with experimental results within 10% deviation (Supporting Information).

Next, we identify the physical origin of the labeled modes. The U-shaped resonator is a typical SRR and has been extensively studied due to its negative refraction properties.[22,32] It has three resonance modes from high to low energy as shown in Figure 1c: the higher order magnetic resonance ($M_{\text{h-order}}$ modes, highlighted by the solid blue line in Figure 1b), fundamental electric resonance ($E(y)$ modes, highlighted by dash green line in Figure 1b, y represents the polarization direction of incident light), and fundamental magnetic modes ($M(z)$, highlighted by solid red line in Figure 1b, z represents the direction of magnetic dipole moment). Here, we identify the highest frequency mode as the higher order magnetic resonance[14] rather than electric plasmon mode.[33] From the dipole current distribution simulated by FDTD as shown in Figure 1c and Figure S2, one can see that the $M_{\text{h-order}}$ modes have a partial circular current, which leads to a magnetic-dipole moment normal to the SRR plane. This is because the electric field of horizontally polarized incident light can couple to the capacitance of the SRR and induce a circulating current in the coil.[14] On the basis of the

simulation results shown in Figure S2, we conclude that $M_{h\text{-}order}$ and $M(z)$ modes can only be excited at the P_x polarization configuration (electric field vector of incident laser is along the x-direction), while $E(y)$ mode can only be excited at the P_y polarization configuration.

The analysis of U-shaped resonator can be applied to interpret the other shapes. For instance, the Y-shaped resonator can be regarded as two connected U-shaped resonators rotated by 90°. The modes in the isolated U shape will couple together and lead to new modes in the combined shapes. The solid blue line highlights the size-dependent evolution of the coupled higher order magnetic mode $M_{h\text{-}order}$, which is induced by P_x polarized light and shows more complex current distribution as shown in Figure 1c and Figure S3b. The P_x and P_y polarizations of incident light induce a couple of degenerated electric modes $E_{sym}(x)$ and $E_{sym}(y)$ corresponding to the valleys highlighted by the green solid and dashed lines in Figure 1b, respectively. This is supported by our simulation (Figure S3). However, experimentally we have observed the mode splitting as the Y-shaped resonator size increases, which are highlighted by the green solid and dashed lines in Figure 1b. We speculate that as the size increases the degeneracy is lifted due to non-ideal symmetry of the two U-shaped resonators. For magnetic modes, the fundamental magnetic dipole modes in each U-shaped resonator couple together, resulting in the two degenerate symmetrically coupled magnetic dipoles modes ($M_{sym,x}(z)$ and $M_{sym,y}(z)$) and one asymmetric mode $M_{asym}(z)$. As there is a phase retardation between two 90°-rotated U structures in the Y shape, the coupling between two magnetic dipoles leads to the spectral splitting of resonance.[35] On the basis of the dipole−dipole coupling theory,[32] the north and the south poles of the two neighboring magnetic dipoles repel each other in the symmetric mode, leading to the longer wavelength $M_{asym,y}(z)$ mode (highlighted as the dashed red line in Figure 1b under a P_y excitation) further red-shifted to beyond the spectral range of our spectrometer, particularly to those resonator with size larger than ~60 nm. In a P_x polarization excitation, only $M_{sym,x}(z)$ mode is observed (solid pink line in Figure 1b). With a similar argument, the spectra of coupled magnetic modes ($M_{sym,x}(z)$ and $M_{sym,y}(z)$) also split into two as the size increases.

Once we understand the physical pictures of those two resonators, we can readily address the mode identifications for other four resonators. The S- and H-shaped resonators can be considered as two 180°-rotated U-shaped resonator configurations connected side-by-side and back-to-back, respectively. The electric (magnetic) dipole−dipole coupling can also form new coupled electric (magnetic) modes. In the S shape, we observed four resonance modes as highlighted by solid blue, dash green, dash pink and solid red lines in Figure 1b, which are respectively identified as higher-order magnetic resonance mode $M_{h\text{-}order}$, symmetrically coupled electric modes $E_{sym}(x)$, asymmetrically coupled electric modes $E_{asym}(x)$, and asymmetrically coupled magnetic mode $M_{asym}(z)$ as subsequently shown in Figure 1c. The $E_{asym}(y)$ mode is very weak and even unresolved when the bar-width is smaller than 50 nm; however, it becomes pronounced for larger size resonators (highlighted by pink dashed line). In the H shape, besides $M_{h\text{-}order}$, $E_{sym}(y)$, and $M_{asym}(z)$ modes, we also observed an asymmetrically coupled electric mode of $E_{asym}(y)$ in the P_y polarization excitation, which is completely dark and decoupled from the normal incident light if the metamolecule exhibits spatial inversion/reflection symmetry, such as the U shape, in the plan of structure.[1] Here, we propose that the observation of $E_{asym}(y)$ in the H-shaped metamaterial is due to the coupling effects between two 180°-rotated U-shaped resonators in one H shape. As there is no phase retardation between the two 180°-rotated U pairs, only a single asymmetric magnetic resonance can be observed in the S and H shapes.[18] The U-bar structure, which consists of a SRR and a bar, is also known as asymmetric split ring resonators (ASRRs).[3] The higher order magnetic resonance $M_{h\text{-}order}$ shows asymmetric alignment of electric dipoles in both of two vertical arms of SRR, and in both of the bar and the bottom arm of SRR. The electric resonance mode is contributed from two degenerated modes of $E_{sym}(x)$ and $E_{sym}(y)$ with parallel alignment of electric-dipoles along x- and y-direction, respectively. Circulating currents induced by P_x-polarized incident light lead to the magnetic resonance $M(z)$. For the V shape, two resonance modes come from the coupling of two dipoles in the angled arms. The P_y-polarization of light induces symmetric aligned electric dipoles in two arms, resulting in an electric mode $E(y)$. Similar with asymmetric coupling in two noncontacted nanowires,[2] the displacement current of asymmetric coupled dipoles between two arms of the V shape also has partial circulating features along the V shape, leading to a resonant excitation of magnetic dipole moment $M(z)$.

Dispersion of ESSPs-like Modes and MSSPs-like Modes. On the basis of Drude model, the frequency of bulk plasma ω_p is depending on the electron density n and effective mass m_e of electrons:[2] $\omega_p = (4\pi ne^2/m_e)^{1/2}$. In metals, the plasma energy is on the order of 10 eV. For instance, it is 9 eV in perfect crystalline gold, 9.2 eV in perfect crystalline silver, and 15 eV in perfect crystalline aluminum.[2,7,34] The dispersion of bulk plasma has the format of[2,34]

$$\omega^2 = \omega_p^2 + c^2k^2 \quad (1)$$

where c is velocity of light in free space, and k is wave vector of light. Equation 1 leads to two results: The first is that there is a threshold frequency at zero wave vector, and the second is that light cannot propagate in

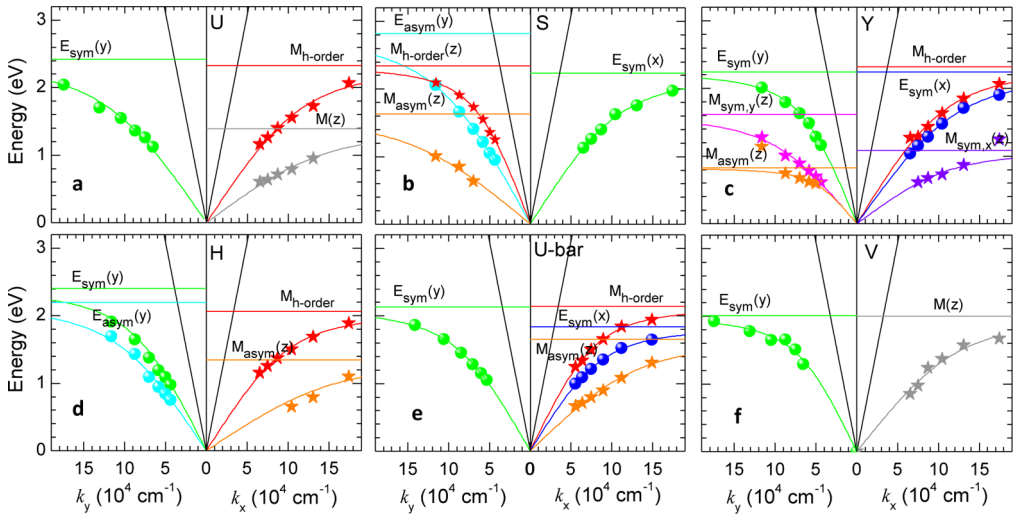

Figure 2. Dispersion of resonance modes. Panels show the dispersion of light (black line), electronic modes (solid spheres), magnetic modes (solid stars), and nondispersive classical surface plasmons (horizontal color lines) along the wave vector of k_x and k_y direction for six alphabetical metamaterials, respectively. The same color corresponds to the same type of resonance modes as shown in Figure 1. The color curves are the fitted results by eq 2. Perfect consistence of all fittings between theory and experiments shows all of modes are surface plasmon polaritons.

the metal when the frequency is below ω_p. For the light with frequency higher than ω_p, usually in the UV range, the metal became transparent. In the presence of a planar boundary, there is a new mode, *i.e.*, surface plasmons, of which the frequency is $\omega_{sp} = \omega_p/(2)^{1/2}$ at the wave vectors k that is much higher than ω_{sp}/c. In the retardation region, where the phase velocity ω_{sp}/k of SPs is comparable to the velocity of light, the surface plasmons couple with the free electromagnetic field and form the surface plasmon polaritons following the dispersion relationship:[2]

$$\omega_{spp}^2(k) = \omega_{sp}^2 + v^2k^2 - \sqrt{\omega_{sp}^4 + v^4k^4} \qquad (2)$$

where v is the effective velocity of light in the interface between metal surface and surround dielectrics, k is the wave vector of SPPs. Equation 2 means that the SPPs propagate along the metal surface with frequencies ranging from zero (k = 0) toward the cutoff frequency corresponding the classical nondispersive surface plasmon ω_{sp}. Since $v \leq c$, the dispersion relation $\omega_{spp}(k)$ always relies on the right part of the light dispersion $\omega_l(k) = ck$. Therefore, the wave vector of SPPs is always larger than that of pure light waves of the same frequency. Hence, the SPPs in an ideal surface are nonradiative in nature, which means that it cannot decay by emitting a photon, and *vice versa*, light incident on an ideal surface cannot excite the surface plasmon. Nevertheless, there are two mechanisms that allow light to be coupled SPPs by providing the momentum mismatch between light and SPPs. The first is attenuated reflection (ATR) which makes use of a prism coupling to increase the momentum of light.[35,36] The second makes use of a periodic surface roughness in metals surface, which can provide the required momentum *via umklapp* processes just like a diffraction grating.[37] Metamaterials have very good periodic surface structure and can easily couple the SPs and light to form SPPs-like modes. In Figure 2, we plot the dispersion relationship of all resonance modes in alphabetical metamaterials. For certain size of metamaterials with a given lattice constant a_i, the resonance energy of corresponding resonance modes can be obtained by measuring the transmission spectra. When we change the size of lattice unit, we obtained the data points of resonance modes energy *versus* lattice constant and, thus, data of the resonance modes energy *versus* vectors. The 2D wave vectors along the surface of metamaterials are inversely proportional to the lattice constant, *i.e.*, $k_i = \pi/a_i$ (i = x, y), where the a_i the lattice constant of metamaterials which can be calculated from the structure parameters as show in Figure S1. For a comparison, we also plot the dispersion of light (black line) and classic nondispersive surface plasmons (colored horizontal line). We found that all of electronic and magnetic modes show the dispersion feature of SPPs and can be perfectly fitted by SPPs dispersion function in eq 2. It suggests that those resonance modes result from coupling between the 2D localized surface plasmon and the free propagating light, leading to the coupling modes of SPP-like. There are two types of SPP-like modes, electronic-surface-plasmon-polaritons-like modes (ESPP-like modes) and magnetic-plasmon-polaritons-like modes (MSPP-like modes). In the coupling process of the ESPP-like modes, the light energy scattered by one metamolecule can be collected by neighboring metamolecule as localized plasmons and are called lattice plasmons.[38−40] For the magnetic modes, it is propagating wave *via* magnetic dipoles for wave propagation along the magnetic-dipole direction. These

magnetization waves are the classical analogue of spins. When these magnetic waves in the 2D structure are coupled with the incident electromagnetic waves, the resonance modes show 2D polaritons-like properties.[18,41,42] Figure 2 indicates that we almost push the frequency of ESPP and MSPPs into the cutoff limit, which covers nearly the entire range of visible to near-infrared optical frequency.

Analysis of dispersion of SPPs provides more insights in advanced applications, such as negative refraction and enhanced sensing capability. The refractive index n depends on the electronic permittivity ε and magnetic permeability μ: $n^2 = \varepsilon\mu$. If both permittivity and permeability are negative, the resulting refractive index is negative as well. The permittivity is usually negative in any metals from zero frequency to the plasma frequency; however, a negative permeability at optical frequency, in particular, does not occur in nature materials. The permeability can be written as[2,43]

$$\mu(\omega) = 1 + \frac{F\omega^2}{\omega_{\text{mspp}}^2 - \omega^2} \quad (3)$$

where F is the filling factor defined by $F = (l_x l_y t_z)/(a_x a_y a_z)$, l_x and l_y are the length of individual metallic "atom" along x- and y-direction, respectively, t_z is the thickness of individual metallic "atom", and $a_{x,y,z}$ is the lattice constant along x-, y-, and z-direction. In our 2D alphabetical metamaterials, there is $t_z = a_z$. On the basis of parameters listed in Figure S1, we have calculated F to be ~50%. To substitute F into eq 3, we obtain that the negative permeability requires $\omega > (2)^{1/2}\omega_{\text{mspp}}$. Our metamaterials can push the magnetic response of high order magnetic modes to 564 nm and fundamental magnetic modes to 668 nm in visible; therefore, in principle, we can push the negative permeability down to 564 nm, with a bandwidth up to $(2)^{1/2}\lambda_{\text{mspp}}$, where λ_{mspp} is the MSPP-like mode wavelength. Besides, the negative refractive index is strongly dependent on the polarization because magnetic mode is necessary. For U, H, U-bar, and V shapes, the negative refraction exists in the x-polarization, while it is in the y-polarization for S shape. The Y shape structures should exhibit negative refraction in both of the polarizations.

Verification of Enhanced Light-Matter Interactions by Tuning the Laser Wavelength. Alphabetical metamaterials operated in visible-IR exhibit abundant electric and magnetic dipole modes, and their coupling effect gives further degree of freedom to tune the plasmonic resonance to optimize the SERS effect. The versatile tunability enables the maximization of the strength of local electromagnetic field hot-spots, which dominate the electromagnetic enhancement in sensing. Next, we will use SERS to test the sensing capability of this tunable alphabetical metamaterials. We first show how to obtain the highest SERS signal by tuning the laser wavelength for the H-shaped metamaterials as an example. Panels a and b of Figure 3 display the typical SERS spectra of a monolayer 2-naphthalenethiol bound to H40 sample excited by a tunable laser with P_x and P_y polarizations, respectively. Considering that laser wavelength (660−840 nm) is far from the first electronic transition (~242 nm) of 2-naphthalenethiol,[37] we propose that the enhancement of SERS signal is entirely contributed by the electromagnetic enhancement. We chose the Raman peak around 1380 cm^{-1} originated from the ring−ring stretching mode to investigate the resonant SERS profile depending on the laser wavelength.[44] Its integrated area intensity is plotted in Figure 3c,d along with the compared data from a H50 sample. By tuning the laser wavelength and polarization to match the corresponding resonant modes in the metamaterials, the enhancement was obtained about 20 times as compared to that of the off-resonance case. On the basis of the Mie scattering theory[5] and resonant SERS effects in nanoparticles,[45] the electromagnetic enhancement factor (EF) is the product of incident light and scattered light enhancement, *i.e.*, $EF_{\text{total}} = EF(\lambda_{\text{laser}}) \times EF(\lambda_{\text{scatt}})$, where $EF(\lambda)$ has the same dispersion relationship with the extinction spectra of metamaterials. In the case of P_x polarization, the $M_{\text{h-order}}$ (~730 nm for H40, and ~820 nm for H50) and $M_{\text{asym}}(y)$ (~1561 nm for H40, and ~1898 nm for H50) were excited (as show in Figure 1b). Because the $M_{\text{asym}}(z)$ mode is far from the excitation laser and the corresponding Stokes shift (1380 cm^{-1}), the stronger signal at higher energy excitation shown in Figure 3c is due to the $M_{\text{h-order}}$ resonance, while in the P_y excitation, two other modes of $E_{\text{sym}}(y)$ (~780 nm for H40, and ~900 nm for H50) and $E_{\text{asym}}(y)$ (~860 nm for H40, and ~1150 nm for H50) are excited. As shown in Figure 3d, two resonant peaks are observed in the H40 sample. One resonant peak is very sharp at around 790 nm with a fwhm of ~10 nm. We propose that it is a double resonant process, in which the incident laser at ~785 nm resonates with $E_{\text{sym}}(y)$, while the scattered light at ~887 nm (~1380 cm^{-1}) is also within the resonance of the $E_{\text{asym}}(y)$ mode. The other peak around 710 nm is much broader because only the scattered light around 787 nm (1380 cm^{-1}) can resonate with the $E_{\text{sym}}(y)$ mode. For the H50 sample, the double-resonance is relaxed, which results in one broad resonant peak around 700 nm because its $E_{\text{asym}}(y)$ mode is too broad and far from the scattered light.

Effect of Shape and Size of Metamaterials on Selectively Enhanced Electromagnatic Field. For a given laser wavelength, for instance 785 nm, the enhancement can be maximized by tuning the size and shape of the alphabetical metamaterials. Here, the chosen patterns are U, V, H, S, and Y shaped metamaterials with bar-width ranging from 30 to 50 nm, also functionalized with a monolayer of 2-naphthenethiol molecules. Figure 4a shows a 2D plot of the SERS spectra under two different

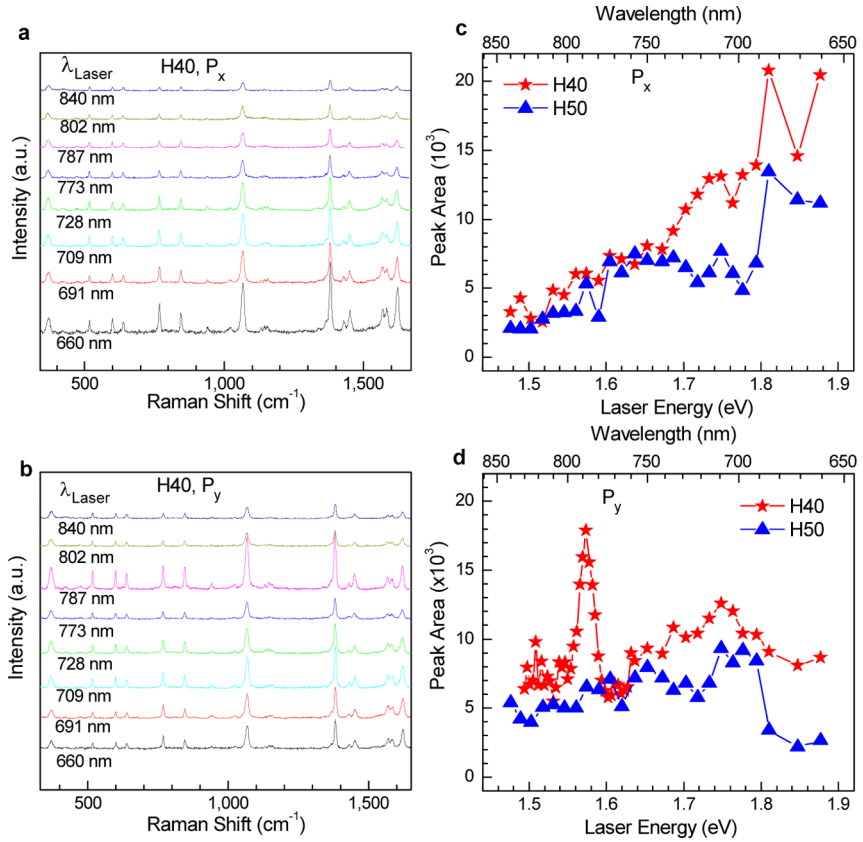

Figure 3. Excitation wavelength dependence of experimental SERS spectra and simulated enhancement spectra at P_x and P_y polarization. Panels a and b are the selected measured SERS spectra, which depend on the laser wavelength for H40 at P_x and P_y polarizations. Panels c and d are laser energy dependence of the integrated intensity (peak area) of ring−ring stretching mode of benzene functional groups at 1380 cm^{-1} for H40 and H50 pattern at two polarization configuration.

polarizations. Bar charts in Figure 4b statistically summarize the simulated and experimental intensities for all different shapes and sizes. It becomes pronounced that the U40, V30, H40, S40, and Y30 samples show much stronger intensities than their other counterparts under a certain polarization. This suggests the versatility and tunability of metamaterials for a known laser excitation in order to gain the highest SERS effect. The explanation can be supported by the simulation of the local electric field distribution (or saying the hot-spots) as shown in Figure 4c. One can see that both experimental data and simulation agree very well with each other. By comparing the Raman spectra of 2-naphthalenethiol powder and the SERS spectra of a covalently self-assembled monolayer of 2-naphthalenethiol, we could also estimate the average enhancement factors (averaging all area of metamaterials pattern) of experimental SERS spectra which are $\sim 10^6$ to $\sim 10^8$, respectively (see Supporting Information and Figure S4). These enhancement values are strong enough for detecting a few molecules located within proximity of the hot-spots.

Application of Alphabetical Metamaterials for Single Molecule Detection. To demonstrate a specific application in food security, we have detected extremely diluted concentrations of two plasticizers: benzyl butyl phthalate (BBP, $C_{19}H_{20}O_4$) and bis(2-ethylhexyl)-phthalate (DEHP, $C_{24}H_{38}O_4$). The plasticizers are known as endocrine disrupters that produce reproductive and developmental toxicity, such as miscarriage, fewer motile sperm, and external sex organs malformation of infant.[46] Figure 5 shows the SERS spectra for the ultrasensitive detection of BBP and DEHP with concentrations from nanomolar to femtomolar level. The femtomolar detection is much lower than the exposure limit of 6 ppb (10^{-9} M/L) in drinking water allowed by Environmental Protection Agency of the United States. In a typical measurement, 40 μL of sample solution was dropped and spread over a 2 $\times$ 2 cm^2 area of the metamaterials. SERS measurements were conducted after the chip was dried in air. As shown in Figure 5a, the overall SERS fingerprint intensity is quantitatively increased with the concentrations of BBP from 1 fM to 1 nM. The Raman peaks at 1066, 1580, and 1618 cm^{-1} correspond to the ring−ring stretching vibration of ortho-phenyl group, and the peaks at 598, 639, and 766 cm^{-1} are from ring deformation. The peaks at 844, 1378, and 1450 cm^{-1} have been assigned to the aromatic C−H twisting vibration, the CH_3 symmetric deformation, and the C−H in plane bending of alkyl group, respectively.[44,47,48] We also conducted DEHP detection from nanomolar to femtomolar level and

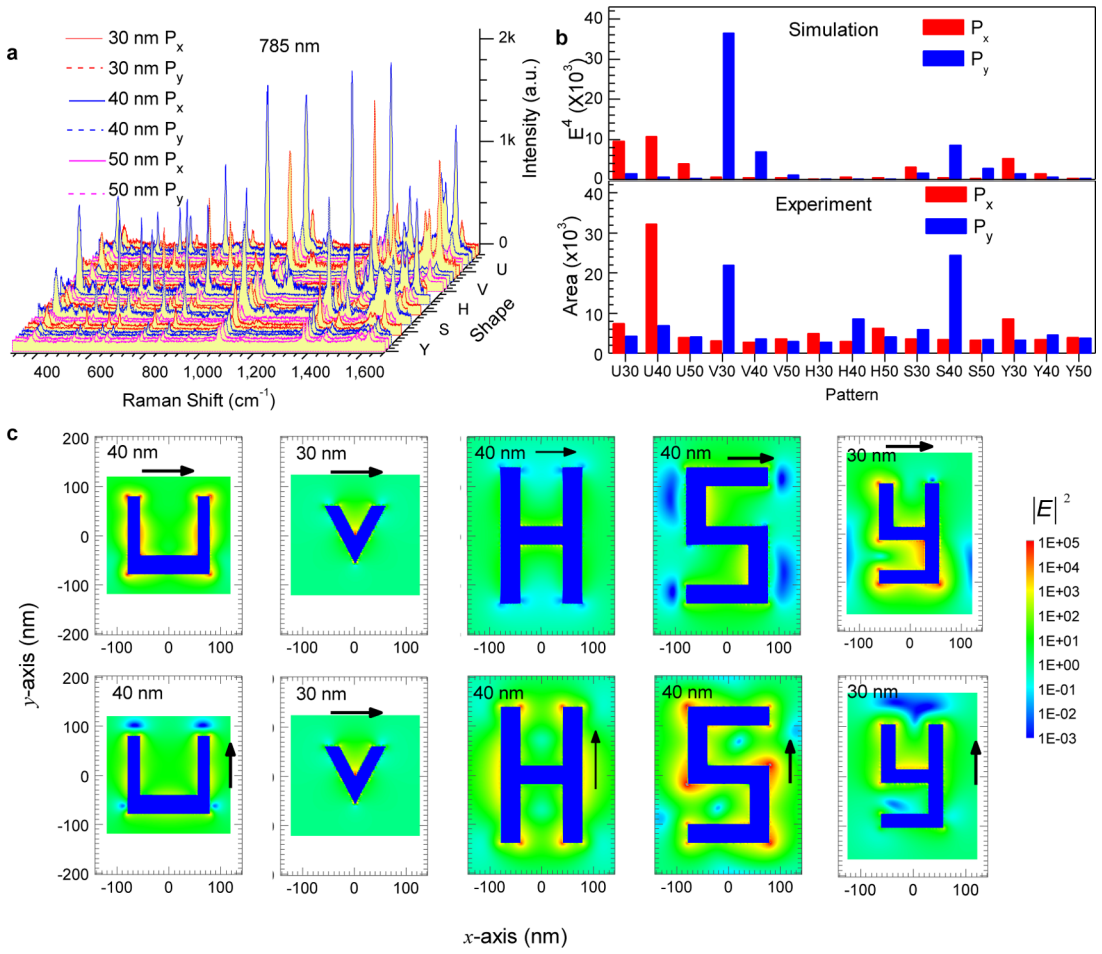

Figure 4. Shape tunable SERS spectra and simulation results at 785 nm excitation. (a) The experimental SERS spectra depending on the shape and width (w = 30 nm for red line, w = 40 nm for blue line, w = 50 nm for pink line) of the alphabetical metamaterials at 785 nm laser with two cross-polarization configurations. The solid lines and the dash lines represent the laser polarizations, which are parallel and vertical to the gap of the alphabet metamaterials, respectively. (b) The statistics results of integrated intensity (area) of experimental SERS spectra at 1380 cm^{-1} peak in (a) and simulated average enhancement factor $|E|^4$ of U, V, S, H and Y shapes from w = 30 nm to w = 50 nm with two polarization configurations. The enhancement factor was calculated based on averaging the $|E|^4$ at 0.5 nm above the structure. The shifting was about 20 nm different-Stoke shift. (c) The simulated contour plot of electronic field intensity of $|E|^2$ for the pattern with the highest enhancement. The black arrows correspond to the laser polarizations. The right corner values are the width w of the SRRs unit.

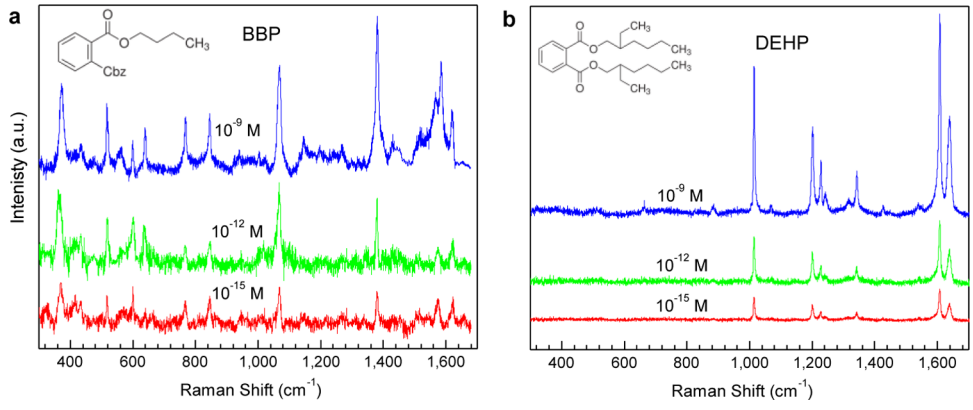

Figure 5. Ultrasensitive SERS detection of plasticizers. (a) The SERS spectra of BBP (benzylbutyl phthalate) and (b) DEHP (bis(2-ethylhexyl)phthalate) molecules for femto- (10^{-15}), pico- (10^{-12}), and nanomolar (10^{-9} mol L^{-1}) levels. Approximately 40 μL of three different concentration of BBP and DEHP was deposited onto 2 × 2 cm^2 H40 metamaterials wafer for SERS measurements. The excitation laser is 785 nm and power is ~1 mW. The acquisition time is 400 s. The laser spot size is about 1 μm^2 for 100× objective.

obtained good signals as shown in Figure 5b. Considering the area ratio of laser spots (~1 μm^2) to metamaterials chip, we can unambiguously conclude that single molecule detection has been obtained (see Supporting Information). Nevertheless, it is still a big challenge to increase the throughput since a handful of molecules spread through all over the substrate. One possibility is to employ superhydrophobic substrate[49] incorporated with metamaterials, which could be a potential solution to concentrate the very low number of molecules onto the active SERS surfaces.

CONCLUSION

In conclusion, by using tunable alphabetical metamaterials operated in the optical frequency, we have demonstrated a detailed study on plasmonic coupling, dispersion of ESPPs and MSPPs, and negative refraction, as well as the ultrasensitive SERS sensing. The optical responses can be readily tailored in vis-NIR range by controlling the size, symmetry, and topology of the unit cell. The dispersion analysis shows that all of resonance modes are 2D surface plasmon polaritons due to the grating-like structures and comparable wave vectors with lights. Hence, the light can be coupled very easily with electronic and magnetic surface plasmons, and thus, the alphabetical metamaterials exhibit a potential negative refractive index in visible optical frequency and an enhanced confinement and concentration of electromagnetic fields in vis-NIR frequency. A series of tunable SERS experiments by tuning the laser wavelength and resonance frequency confirm the ultrasensitive capability and can readily detect the mononlayer molecules and ultradilute plasticizer solution as low as femtomolar concentration. Our study on the tunable alphabetical metamaterials will open a wide range of possibility for the fabrication of visible plasmonic metamaterials to benefit potential applications in invisible cloaking, nonlinear optics, negative refraction, transforming optics, and sensing.

METHODS

Fabrication of Alphabetical Metamaterials. The metamaterials with different bar widths from 30 to 80 nm were fabricated on 0.7 mm-thick ITO/glass substrates over an area of 40 μm × 40 μm by electron beam lithography (EBL). Commercial electron beam resist poly(methyl methacrylate) was spin-coated at 4000 rpm for 1 min on the ITO/glass and baked at 180 °C for 20 min. The metamaterials patterns (geometrical parameters and periodicity of the unit cell are described in the Supporting Information Figure S1) were produced using a JEOL 7001 F SEM equipped with a nanometer pattern generation system (NPGS), and then developed in 1:3 methyl isobutyl ketone/isopropyl alcohol (MIBK/IPA) developer for 90 s. After the development, 30 nm Au film following a 2 nm Cr as an adhesive layer was deposited using thermal evaporation deposition (Elite Engineering, Singapore) at a base pressure of 3×10^{-7} Torr. Finally, the sample was immersed in acetone for at least 3 h for separation and washed thoroughly with IPA and water.

Transmission and SERS Measurements. To evaluate the resonance modes of alphabetical metamaterials, the transmission spectra were conducted using a microspectrophotometer (Craic 20) in the range of 400−2100 nm. The laser tunable SERS spectroscopy was performed in a back scattering geometry using a Jobin-Yvon HR800 Raman system equipped with a liquid nitrogen-cooled charge-coupled detector (CCD). The laser excitation wavelengths are selected from a Ti-Sapphire laser (Coherent). We use a continually tunable Notch filter to reject the laser line, and thus, there was no need to change the filters for different wavelengths we used. For pattern tunable experiments (Figure 4), Jobin-Yvon T64000 was used in a back scattering geometry excited by a diode laser (λ = 785 nm). For all SERS experiments, the laser power was kept bellow 1 mW unless otherwise stated. For the laser tunable SERS spectroscopy (Figure 3), an important step is to calibrate the wavelength-dependent laser flux and the system response. We used a silicon wafer with ⟨111⟩ orientation as a standard sample for the calibration of the laser flux, while we used a standard tungsten halogen light source (HL-2000, Ocean Optics) to calibrate the system response.

DDA and FDTD Simulation. The transition spectra of alphabetical metamaterials is simulated by discrete dipole approximation (DDA) method using the DDSCAT program (version 7.0).[34,35] Two nanometer grids were used for all simulations. The shape involved in the experiment is too complex. For the effective medium, we tried to avoid the complexity by using a simple box with dimensions of 30 × 120 × 120 nm (height × width × length) put on top of ITO (refractive index of 1.9). The effective medium is equivalent to the total of each surface in relative to the refractive index (air or ITO) divided by the total amount of box surface. Figure S3a is calculated using FDTD method; the geometries of each structure were directly imported based on the SEM micrograph, which allows us to simulate a closer shape available in experiment. Subsequently, the same structure of alphabetical metamaterials was used to calculate the dipole current distribution at their respective resonance peak, which is shown in Figure S3b.

Conflict of Interest: The authors declare no competing financial interest.

Acknowledgment. The author Q.X. thanks the strong support from Singapore National Research Foundation through a Fellowship grant (NRF-RF2009-06), the support from Singapore Ministry of Education *via* two Tier 2 grants (MOE2011-T2-2-085 and MOE2011-T2-2-051), and a very strong support from Nanyang Technological University *via* start-up grant (M58110061). X.X. acknowledges Natural Science Basic Research Plan in Shaanxi Province of China (No. 2012KJXX-27). S.L. acknowledges the support from Singapore Ministry of Education *via* Tier 2 grants (MOE2011-T2-2-085) and the support from Nanyang Technological University *via* start-up grant. P.T. acknowledges the support from the special funds for Major State Basic Research of China, Contract No. 2009CB929301, and the National Natural Science Foundation of China, Grants No. 11225421 and No. 10934007.

Supporting Information Available: Geometrical parameters and periodicity of the unit cell (Figure S1); simulated extinction spectra depending on the dimensions of selected metamolecule units (Figure S2); FDTD simulation of transmission spectra and corresponding dipole current distributions (Figure S3); experimental estimation of enhancement factor (Figure S4 and Table S1). This material is available free of charge *via* the Internet at http://pubs.acs.org.

REFERENCES AND NOTES

1. Schuller, J. A.; Barnard, E. S.; Cai, W.; Jun, Y. C.; White, J. S.; Brongersma, M. L. Plasmonics for extreme light concentration and manipulation. *Nat. Mater.* **2010**, *9*, 193–204.

2. Pitarke, J. M.; Silkin, V. M.; Chulkov, E. V.; Echenique, P. M. Theory of surface plasmons and surface-plasmon polaritons. *Rep. Prog. Phys.* **2007**, *70*, 1–87.
3. Barnes, W. L.; Dereux, A.; Ebbesen, T. W. Surface plasmon subwavelength optics. *Nature* **2003**, *424*, 824–830.
4. Wei, H.; Zhang, S.; Tian, X.; Xu, H. Highly tunable propagating surface plasmons on supported silver nanowires. *Proc. Natl. Acad. Sci. U.S.A.* **2013**, *110*, 4494–4499.
5. Anker, J. N.; Hall, W. P.; Lyandres, O.; Shah, N. C.; Zhao, J.; Van Duyne, R. P. Biosensing with plasmonic nanosensors. *Nat. Mater.* **2008**, *7*, 442–453.
6. Kabashin, A. V.; Evans, P.; Pastkovsky, S.; Hendren, W.; Wurtz, G. A.; Atkinson, R.; Pollard, R.; Podolskiy, V. A.; Zayats, A. V. Plasmonic nanorod metamaterials for biosensing. *Nat. Mater.* **2009**, *8*, 867–871.
7. Hess, O.; Pendry, J. B.; Maier, S. A.; Oulton, R. F.; Hamm, J. M.; Tsakmakidis, K. L. Active nanoplasmonic metamaterials. *Nat. Mater.* **2012**, *11*, 573–584.
8. Kauranen, M.; Zayats, A. V. Nonlinear plasmonics. *Nat. Photonics* **2012**, *6*, 737–748.
9. Nie, S. M.; Emery, S. R. Probing single molecules and single nanoparticles by surface-enhanced Raman scattering. *Science* **1997**, *275*, 1102–1106.
10. Kleinman, S. L.; Ringe, E.; Valley, N.; Wustholz, K. L.; Phillips, E.; Scheidt, K. A.; Schatz, G. C.; Van Duyne, R. P. Single-molecule surface-enhanced raman spectroscopy of crystal violet isotopologues: Theory and experiment. *J. Am. Chem. Soc.* **2011**, *133*, 4115–4122.
11. Shen, Y.; Zhou, J.; Liu, T.; Tao, Y.; Jiang, R.; Liu, M.; Xiao, G.; Zhu, J.; Zhou, Z.-K.; Wang, X.; *et al.* Plasmonic gold mushroom arrays with refractive index sensing figures of merit approaching the theoretical limit. *Nat. Commun.* **2013**, *4*, 2381–2389.
12. Ling, X.; Xie, L.; Fang, Y.; Xu, H.; Zhang, H.; Kong, J.; Dresselhaus, M. S.; Zhang, J.; Liu, Z. Can graphene be used as a substrate for Raman enhancement? *Nano Lett.* **2009**, *10*, 553–561.
13. Schurig, D.; Mock, J. J.; Justice, B. J.; Cummer, S. A.; Pendry, J. B.; Starr, A. F.; Smith, D. R. Metamaterial electromagnetic cloak at microwave frequencies. *Science* **2006**, *314*, 977–980.
14. Enkrich, C.; Wegener, M.; Linden, S.; Burger, S.; Zschiedrich, L.; Schmidt, F.; Zhou, J. F.; Koschny, T.; Soukoulis, C. M. Magnetic metamaterials at telecommunication and visible frequencies. *Phys. Rev. Lett.* **2005**, *95*, 203901.
15. Xu, X.; Peng, B.; Li, D.; Zhang, J.; Wong, L. M.; Zhang, Q.; Wang, S.; Xiong, Q. H. Flexible visible−infrared metamaterials and their applications in highly sensitive chemical and biological sensing. *Nano Lett.* **2011**, *11*, 3232–3238.
16. Shelby, R. A.; Smith, D. R.; Schultz, S. Experimental verification of a negative index of refraction. *Science* **2001**, *292*, 77–79.
17. Pendry, J.; Holden, A.; Robbins, D.; Stewart, W. Magnetism from conductors and enhanced nonlinear phenomena. *IEEE Trans. Microwave Theory Tech.* **1999**, *47*, 2075–2084.
18. Liu, N.; Giessen, H. Coupling effects in optical metamaterials. *Angew. Chem., Int. Ed.* **2010**, *49*, 9838–9852.
19. Zhang, Q.; Wen, X.; Li, G.; Ruan, Q.; Wang, J.; Xiong, Q. H. Multiple magnetic mode-based fano resonance in split-ring resonator/disk nanocavities. *ACS Nano* **2013**, *1*, 11071–11078.
20. Fan, J. A.; Wu, C.; Bao, K.; Bao, J.; Bardhan, R.; Halas, N. J.; Manoharan, V. N.; Nordlander, P.; Shvets, G.; Capasso, F. Self-Assembled Plasmonic Nanoparticle Clusters. *Science* **2010**, *328*, 1135–1138.
21. Prodan, E.; Radloff, C.; Halas, N. J.; Nordlander, P. A hybridization model for the plasmon response of complex nanostructures. *Science* **2003**, *302*, 419–422.
22. Linden, S.; Enkrich, C.; Wegener, M.; Zhou, J.; Koschny, T.; Soukoulis, C. M. Magnetic response of metamaterials at 100 terahertz. *Science* **2004**, *306*, 1351–1353.
23. Dumelow, T.; Oliveros, M. C. Continuum model of confined magnon polaritons in superlattices of antiferromagnets. *Phys. Rev. B* **1997**, *55*, 994–1005.
24. Lin, J.; Mueller, J. P. B.; Wang, Q.; Yuan, G.; Antoniou, N.; Yuan, X.-C.; Capasso, F. Polarization-controlled tunable directional coupling of surface plasmon polaritons. *Science* **2013**, *340*, 331–334.
25. Yin, X.; Ye, Z.; Rho, J.; Wang, Y.; Zhang, X. Photonic spin hall effect at metasurfaces. *Science* **2013**, *339*, 1405–1407.
26. Haggui, M.; Dridi, M.; Plain, J.; Marguet, S.; Perez, H.; Schatz, G. C.; Wiederrecht, G. P.; Gray, S. K.; Bachelot, R. Spatial confinement of electromagnetic hot and cold spots in gold nanocubes. *ACS Nano* **2012**, *6*, 1299–1307.
27. Cao, C.; Zhang, J.; Wen, X.; Dodson, S. L.; Dao, N. T.; Wong, L. M.; Wang, S.; Li, S.; Phan, A. T.; Xiong, Q. H. Metamaterials-based label-free nanosensor for conformation and affinity biosensing. *ACS Nano* **2013**, *7*, 7583–7591.
28. Wen, X.; Li, G.; Zhang, J.; Zhang, Q.; Peng, B.; Wong, L. M.; Wang, S.; Xiong, Q. H. Transparent free-standing metamaterials and their applications in surface-enhanced Raman scattering. *Nanoscale* **2014**, *6*, 132–139.
29. Liu, N.; Guo, H.; Fu, L.; Kaiser, S.; Schweizer, H.; Giessen, H. Plasmon hybridization in stacked cut-wire metamaterials. *Adv. Mater.* **2007**, *19*, 3628–3632.
30. Rockstuhl, C.; Lederer, F.; Etrich, C.; Zentgraf, T.; Kuhl, J.; Giessen, H. On the reinterpretation of resonances in split-ring-resonators at normal incidence. *Opt. Express* **2006**, *14*, 8827–8836.
31. Liu, N.; Tang, M. L.; Hentschel, M.; Giessen, H.; Alivisatos, A. P. Nanoantenna-enhanced gas sensing in a single tailored nanofocus. *Nat. Mater.* **2011**, *10*, 631–636.
32. Smith, D. R.; Pendry, J. B.; Wiltshire, M. C. K. Metamaterials and negative refractive index. *Science* **2004**, *305*, 788–792.
33. Corrigan, T. D.; Kolb, P. W.; Sushkov, A. B.; Drew, H. D.; Schmadel, D. C.; Phaneuf, R. J. Optical plasmonic resonances in split-ring resonator structures: an improved LC model. *Opt. Express* **2008**, *16*, 19850–19864.
34. Pendry, J. B.; Holden, A. J.; Stewart, W. J.; Youngs, I. Extremely low frequency plasmons in metallic mesostructures. *Phys. Rev. Lett.* **1996**, *76*, 4773–4776.
35. Otto, A. Excitation of nonradiative surface plasma waves in silver by the method of frustrated total reflection. *Z. Phys.* **1968**, *216*, 398.
36. Kretschmann, E.; Raether, H. Radiative decay of nonradiative surface plasmons excited by light. *Z. Naturforsch.* **1968**, *A23*, 2135–2136.
37. Teng, Y.-Y.; Stern, E. A. Plasma radiation from metal grating surfaces. *Phys. Rev. Lett.* **1967**, *19*, 511–514.
38. Hicks, E. M.; Zou, S.; Schatz, G. C.; Spears, K. G.; Van Duyne, R. P.; Gunnarsson, L.; Rindzevicius, T.; Kasemo, B.; Käll, M. Controlling plasmon line shapes through diffractive coupling in linear arrays of cylindrical nanoparticles fabricated by electron beam lithography. *Nano Lett.* **2005**, *5*, 1065–1070.
39. Auguié, B.; Barnes, W. L. Collective resonances in gold nanoparticle arrays. *Phys. Rev. Lett.* **2008**, *101*, 143902.
40. Zhou, W.; Odom, T. W. Tunable subradiant lattice plasmons by out-of-plane dipolar interactions. *Nat. Nanotechnol.* **2011**, *6*, 423–427.
41. Dolling, G.; Wegener, M.; Schädle, A.; Burger, S.; Linden, S. Observation of magnetization waves in negative-index photonic metamaterials. *Appl. Phys. Lett.* **2006**, *89*, 231181–231183.
42. Liu, H.; Liu, Y. M.; Li, T.; Wang, S. M.; Zhu, S. N.; Zhang, X. Coupled magnetic plasmons in metamaterials. *Phys. Status Solidi B* **2009**, *246*, 1397–1406.
43. Linden, S.; Enkrich, C.; Dolling, G.; Klein, M. W.; Zhou, J.; Koschny, T.; Soukoulis, C. M.; Burger, S.; Schmidt, F.; Wegener, M. Photonic metamaterials: Magnetism at optical frequencies. *IEEE J. Sel. Top. Quantum Electron.* **2006**, *12*, 1097–1105.
44. Alvarez-Puebla, R. A.; Dos Santos, D. S.; Aroca, R. F. Surface-enhanced Raman scattering for ultrasensitive chemical analysis of 1 and 2-naphthalenethiols. *Analyst* **2004**, *129*, 1251–1256.
45. Willets, K. A.; Van Duyne, R. P. Localized surface plasmon resonance spectroscopy and sensing. *Annu. Rev. Phys. Chem.* **2007**, *58*, 267–297.

46. Lyche, J. L.; Gutleb, A. C.; Bergman, A.; Eriksen, G. S.; Murk, A. J.; Ropstad, E.; Saunders, M.; Skaare, J. U. Reproductive and developmental toxicity of phthalates. *J. Toxicol. Environ. Health, Part B* **2009**, *12*, 225–249.
47. Norbygaard, T.; Berg, R. W. Analysis of phthalate ester content in poly(vinyl chloride) plastics by means of Fourier transform Raman spectroscopy. *Appl. Spectrosc.* **2004**, *58*, 410–413.
48. Peng, B.; Li, G.; Li, D.; Dodson, S.; Zhang, Q.; Zhang, J.; Lee, Y. H.; Demir, H. V.; Yi Ling, X.; Xiong, Q. H. Vertically aligned gold nanorod monolayer on arbitrary substrates: Self-assembly and femtomolar detection of food contaminants. *ACS Nano* **2013**, *7*, 5993–6000.
49. De Angelis, F.; Gentile, F.; Mecarini, F.; Das, G.; Moretti, M.; Candeloro, P.; Coluccio, M. L.; Cojoc, G.; Accardo, A.; Liberale, C.; *et al.* Breaking the diffusion limit with super-hydrophobic delivery of molecules to plasmonic nanofocusing SERS structures. *Nat. Photonics* **2011**, *5*, 682–687.